

Supporting Information:

The role of OH intermediates during the Au oxide electro-reduction at low pH elucidated by EC-SERS and implicit solvent DFT

Authors:

Jonas H. K. Pfisterer,¹ Francesco Nattino,² Ulmas E. Zhumaev,¹ Manuel Breiner,¹ Juan M. Feliu,³ Nicola Marzari,² and Katrin F. Domke^{1,}*

Affiliations:

1 – Molecular Spectroscopy Department, Max Planck Institute for Polymer Research, Ackermannweg 10, 55128 Mainz, Germany

2 – Theory and Simulations of Materials (THEOS) and National Centre for Computational Design and Discovery of Novel Materials (MARVEL), École Polytechnique Fédérale de Lausanne, 1015 Lausanne, Switzerland

3 – Instituto de Electroquímica, Universidad de Alicante, Apdo. 99, 03080 Alicante, Spain

* Corresponding Author: Tel: +49 (0) 6131 379-476, Email: domke@mpip-mainz.mpg.de

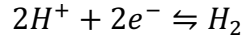
Stability considerations of DFT computed interface structures

The relative stability of the simulated interfaces can be estimated by comparing the formation free energies of the corresponding structures, ΔG_{form} . In particular, ΔG_{form} is computed from the chemical potentials of the relevant species, as available in the electrochemical environment. For a structure that forms from gold and oxygen atoms, protons and electrons, we can formally write ΔG_{form} as:

$$\Delta G_{form} = E_{int} + G^{vib} - N_{Au}\mu_{Au} - N_O\mu_O - N_{H^+}\mu_{H^+} - N_{e^-}\mu_{e^-} \quad (1)$$

Here, E_{int} is the DFT total energy of the interface structure, G^{vib} is the vibrational free energy contribution (computed according to the harmonic approximation), N_X is the number of species X required to form the interface and μ_X the corresponding chemical potential.

The computational hydrogen electrode (CHE) approach originally proposed by Nørskov and coworkers¹ provides a strategy to efficiently estimate the chemical potential of the solvated protons, μ_{H^+} . In particular, the CHE exploits the fact that at 0 V vs. SHE and standard conditions, the following reaction is in equilibrium:



Thus, μ_{H^+} can be computed from the chemical potential of H_2 , μ_{H_2} , as:

$$\mu_{H^+} = \frac{1}{2}\mu_{H_2} - k_B T \ln 10 + U_0 \quad (2)$$

where U_0 is the potential of the standard hydrogen electrode on an absolute scale and the second term on the r.h.s of equation (2) represents an entropic contribution related to the concentration of H^+ in the solution.

The electron chemical potential μ_{e^-} at a given applied bias U is given by:

$$\mu_{e^-} = -e(U + U_0) \quad (3)$$

In the original CHE formulation, only proton-coupled electron transfers are assumed to take place, i.e. equations (2) and (3) are actually combined in an effective hydrogen chemical potential:¹

$$\mu_H = \mu_{H^+} + \mu_{e^-} = \frac{1}{2}\mu_{H_2} - k_B T \ln 10 - eU \equiv \mu_H(U) \quad (4)$$

Note that U_0 has dropped out, so that μ_H only depends on the applied bias vs. SHE, i.e. U . The chemical potential of (gaseous) H_2 at a given temperature and pressure can be calculated from DFT total energy calculations using standard techniques for ideal gases. In particular, we have taken into account (harmonic) vibrational, translational and rotational contributions, and considered a H_2 partial pressure of 101325 Pa.

The chemical potentials of atomic oxygen can be related to the chemical potential of water, which is assumed to represent its reservoir:

$$\mu_O = \mu_{H_2O} - 2\mu_H \quad (5)$$

The chemical potential of (liquid) water, μ_{H_2O} , in turn, is calculated as the chemical potential of an ideal gas at a pressure corresponding to the water vapor pressure (3534 Pa), representing the pressure at which liquid and vapor water are in equilibrium.

Finally, the chemical potential of gold atoms has been computed as the DFT total energy of bulk Au plus the (harmonic) vibrational free energy contribution:

$$\mu_{Au} = E_{bulk} + G_{bulk}^{vib} \quad (6)$$

The latter has been estimated from the phonons computed for the fcc Au bulk structure using the Phonopy package.²

Thus, the formation free-energy of a given interface can be computed from equations (1-6). The CHE assumption of exclusive proton-coupled electron transfers allows introducing the potential bias-dependence for ΔG_{form} through equation (4), without the need of performing calculations for explicitly charged systems. Figure S1 illustrates the corresponding formation free energies computed for the various interface structures presented in Figure S12.

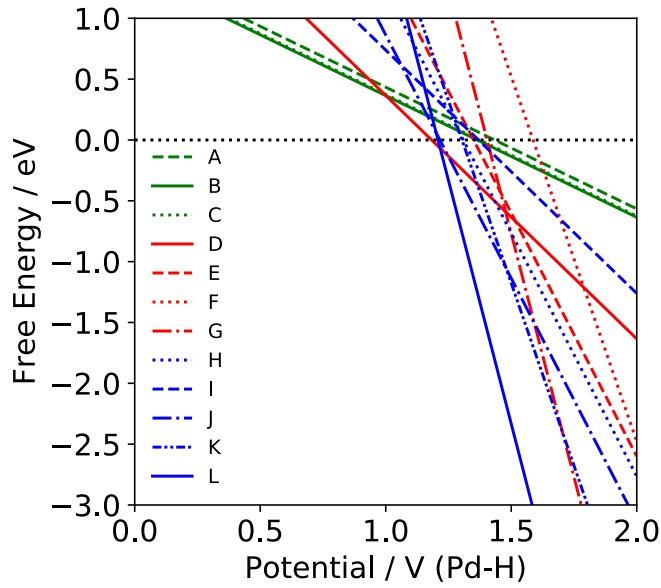


Figure S1. Formation free energy of the various surface-oxidized structures as a function of the potential bias. The clean Au(111) surface is employed as a reference. Red and blue lines correspond to the structures originated from the pristine Au(111) surface and from the roughened surfaces, respectively. The green lines correspond to the structures involving an adsorbed OH species. Interface labels (A-L) are defined in Figure S12.

The CHE approach can be generalized in a grand-canonical framework that allows to decouple potential and pH effects by treating the proton and the electron chemical potentials as free variables.³ Equations (2) and (3) are thus treated independently and not bundled together as in equation (4). In particular, calculations for a given interface structure are performed for different values of the surface charge. The corresponding potential bias is determined *a posteriori* from the difference between the Fermi energy of the system and the asymptotic electrostatic potential. The vacuum level is the natural potential reference for such calculations. It is important to notice at this point that in order to perform accurate predictions in this grand-potential approach, the theoretical framework employed needs to describe well the surface charging as a function of the potential bias and to correctly place the potential of zero charge

(PZC) on the absolute scale employed. In fact, for $N_{H^+} \neq N_{e^-}$, U_0 does not drop out as in equation (4). Concerning the surface charging, the cavity function defining the boundary of the embedding dielectric continuum is known to strongly affect the surface charging as a function of the applied potential and, in turn, the interfacial differential capacitance. The original parametrization of the density-based cavity from the revised self-consistent continuum solvation model (SCCS)⁴ that we have employed in the current work to account for solvent effects has been previously found to strongly underestimate the differential capacitance of Ag(100).^{3,5,6} Similarly, the capacitance computed for a clean Au(111) surface has been found to be significantly lower than corresponding measurements (see Figure S2, where, however, experiments refer to a polycrystalline surface). Instead, the cavity based on atom-centered interlocking spheres from the soft-sphere continuum solvation (SSCS) model⁷ has been found to provide a better description of the experimental capacitance curves (see Figure S2), and, as such, to provide more accurate predictions of the surface charge as a function of the applied potential. We have thus made use of this cavity function for constructing the stability plots illustrated in Figure S3, using the original parametrization of the SSCS model that has been fitted to neutral isolated systems ($\alpha=1.16$, $\Delta = 0.5 \text{ \AA}$). Concerning the ability of the solvation model to correctly place the PZC on an absolute scale, we have introduced an empirical shift of 1.27 eV in order to align the theoretically-computed PZC for Au(111) $U_{PZC}^{SSCS} = 3.64 \text{ V}$ (with respect to the vacuum level) to the corresponding experimental estimate ($U_{PZC}^{exp} = 4.91 \text{ V}$).⁸ Note, the PZC values that are predicted using DFT with implicit solvation models are quite sensitive to the details of the continuum model employed. In particular, moving the onset of the solvent region, occupied by the dielectric continuum, closer to the metal surface, can lead to significant changes of the predicted PZC (even up to 1 V),³ as the screening of the surface dipole is strongly influenced by the distance between the dielectric medium and the surface. Thus, the electrostatic work to extract an electron from the surface is very sensitive to the

parameters that regulate the transition between the continuum and the atomistic regions, and so is the reference of the electrostatic potential on an absolute scale. Note that the continuum model employed for the fully-grand-canonical stability calculations has been selected for the good agreement that it returns with experimental capacitance data, thus ensuring a realistic description of the surface charging as a function of the applied (i.e. relative) potential.

The electrolyte screening of the surface excess charge has been modeled at a continuum level using the size-modified Poisson-Boltzmann theory.^{6,9} The diffuse-layer charge density has been computed self-consistently for a 0.1 M 1:2 electrolyte that mimicked the H₂SO₄ solution employed in the experiments. Steric repulsion between solvated ions has been accounted for^{6,9} using $r = 3.79 \text{ \AA}$ as SO_4^{2-} hydrated ionic radius.¹⁰ The spacing between the slab's periodic images has been increased to 40 \AA in order to provide a sufficient screening length along the surface normal.

Results illustrated in Figure S3 show that for the chosen interface structures and for the potential ranges that are relevant for this work, the full grand-canonical approach predicts very similar stability curves as the CHE, validating the use of the latter for the explored potential range.

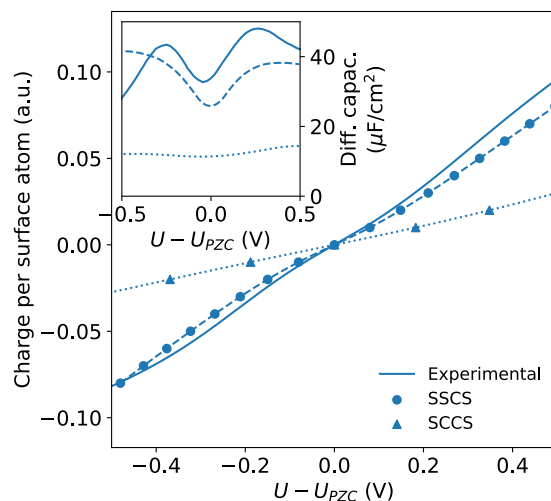


Figure S2. Surface charge density and differential capacitance. Surface charge density and differential capacitance (inset) computed as a function of the potential bias for a clean Au(111) surface. Results of calculations (dashed and dotted curves for SSCS and SCCS cavities, respectively) are compared to experimental data from Ref.¹¹ corresponding to a polycrystalline gold electrode in a 0.05 KClO₄ electrolyte (solid curves). The surface has been modeled as an 8-layer slab, and the vacuum region between periodic slab replicas increased to 120 Å to capture the long-range screening that characterizes the modeled electrolyte concentration. An effective ionic radius $r = 3.38$ Å corresponding to the hydrated ionic radius of ClO₄⁻ has been employed in the simulations.¹⁰ Experimental surface charge densities have been calculated by integrating the capacitance curve from the potential of zero charge (i.e. the capacitance minimum) outward.

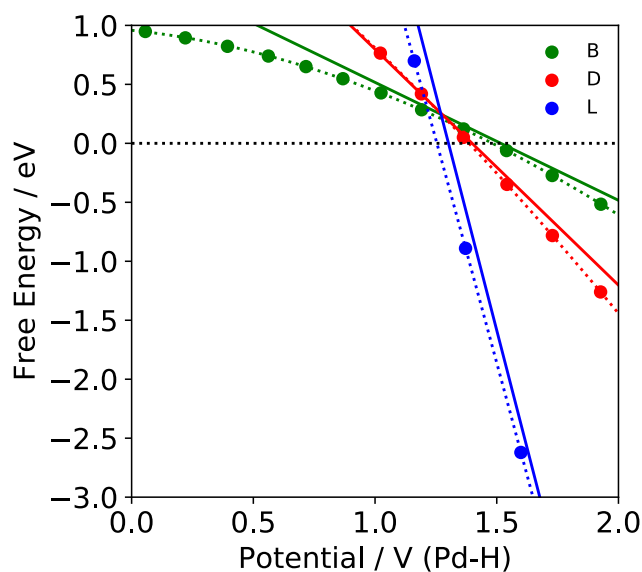
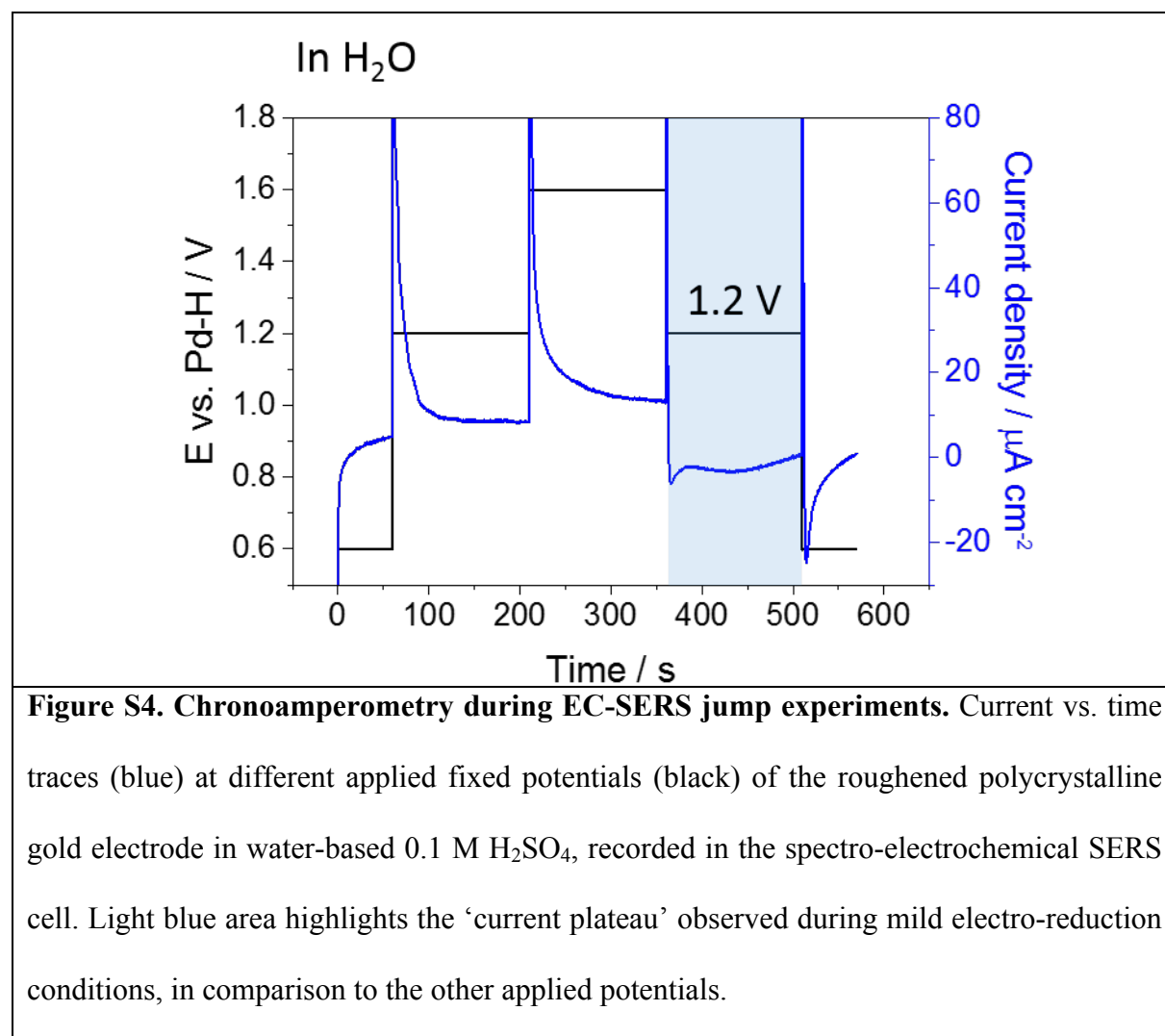


Figure S3. Comparison between computational hydrogen electrode and grand-canonical approaches. Formation free energy for selected surface-oxidized structures as a function of the potential bias. The computational hydrogen electrode approach (solid lines) is compared to calculations using a grand-canonical approach (full dots, dashed lines to guide the eyes). A $\text{pH} = 1$ has been considered, consistently with the experimental conditions. Interface labels (B, D, L) are defined in Figure S12.

Chronoamperometry during simultaneous EC-SERS jump experiments

Figure S4 reports current vs. time traces (blue) at different applied potential-steps (black) of the roughened polycrystalline gold electrode in water-based 0.1 M H_2SO_4 , recorded in the utilized spectro-electrochemical SERS cell (potential sequence: 0.6 V \rightarrow 1.2 V \rightarrow 1.6 V \rightarrow 1.2 V \rightarrow 0.6 V vs. Pd-H) during EC-SERS measurements. The light blue area highlights the ‘current plateau’ observed during the AuOx reduction, when jumping to the AuOx reduction onset (\sim 1.2 V vs. Pd-H). At the other applied potentials, the current vs. time traces reveal an exponential decay. In the main text, Figure 1A shows the corresponding graph for current vs. time traces obtained

in D₂O-based sulfuric acid electrolyte. The 50 mV difference of the CVs (see Figure S5B) is taken into account and the applied potentials are adjusted accordingly.



CV response of polycrystalline gold electrodes in different electrolytes

In Figure S5A, the CVs of the roughened (for EC-SERS enhancement) and not roughened polycrystalline gold electrodes are compared. In general, both CVs portray the same features; however, the electrochemically roughened gold electrode shows higher oxidation and reduction currents, despite the lower scan rate (50 vs. 100 mV/s). The roughening procedure introduces nanostructures that lead to enhancement of the Raman signals due to surface plasmons. Therefore, the roughened electrodes possess higher actual surface areas, as apparent from the

higher oxidation/reduction currents. Nevertheless, the underlying surface electrochemistry is expected to be the same, as both CVs are nearly the same.

Figure S5B shows the CVs for the roughened polycrystalline Au electrodes in water and deuterium based sulfuric acid. The CV in D₂O is shifted by approximately 50 mV. This 50 mV shift is taken into consideration for the EC-SERS potential jump experiments comparing H₂O- and D₂O-based experiments.

Below 0.4 V vs. Pd-H, the CVs in Figure S5A and B show some oxygen reduction activity and subsequent hydrogen peroxide oxidation (the product of the oxygen reduction) around 1.1 V vs. Pd-H (positive sweep). During our EC-SERS potential jump experiments, we utilize potentials significantly greater than 0.4 V vs. Pd-H (see Figure S4) to exclude hydrogen peroxide formation.

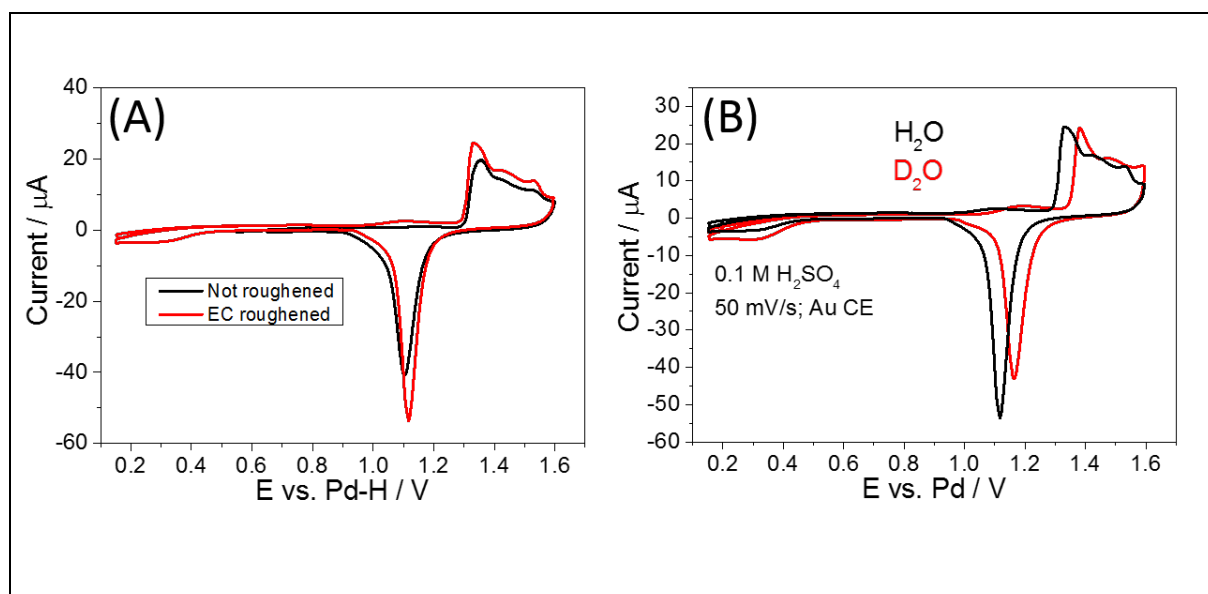


Figure S5. Cyclic Voltammetry of sample electrodes. (A) Comparison between the CVs of the polycrystalline gold electrode (black, scan rate = 100 mV/s) and the roughened polycrystalline gold electrode for EC-SERS experiments (red, scan rate = 50 mV/s) in 0.1 M H₂SO₄. (B) Comparison of CVs of the roughened polycrystalline gold electrode in 0.1 M H₂SO₄ water (black) and deuterium (red) based electrolytes (scan rate = 50 mV/s). The CV is shifted about 50 mV to more positive potentials upon deuteration.

Electrochemical potential jump experiments

To systematically characterize and set up the potential jump experiments combined with EC-SERS, a number of pure electrochemical measurements were conducted on (not roughened) polycrystalline Au electrodes in 0.1 M H₂SO₄ water-electrolyte (Figure S6-S8). As Figure 5A exhibits a slight shift in the AuOx reduction potential of approximately 20 mV, comparing the roughened and not roughened gold electrodes, this potential difference/offset needs to be taken into consideration when comparing purely electrochemical and EC-SERS potential jump experiments.

First, the surface oxidation was investigated by linear potential up-scan to the upper vertex potential (UVP) of 1.6 V, 1.5 V and 1.4 V vs. Pd-H, subsequent potential holding for varied time periods (0-600 s) and a final linear potential down-scan (Figure S6A). The reduction peaks shift to more negative potentials with increasing holding times. The integrated charge profiles reveal a strong current increase during the first 60 s (Figure S6B). For longer waiting times, the charge vs. time curves do not show the expected saturation value of a completely oxidized limited surface area, but show a slow linear increase. This slow linear charge increase might originate from the oxidation of the lower lying gold substrate, as previously observed.¹² A holding time, t_h , of 180 s was chosen for the following additional electrochemical measurements.

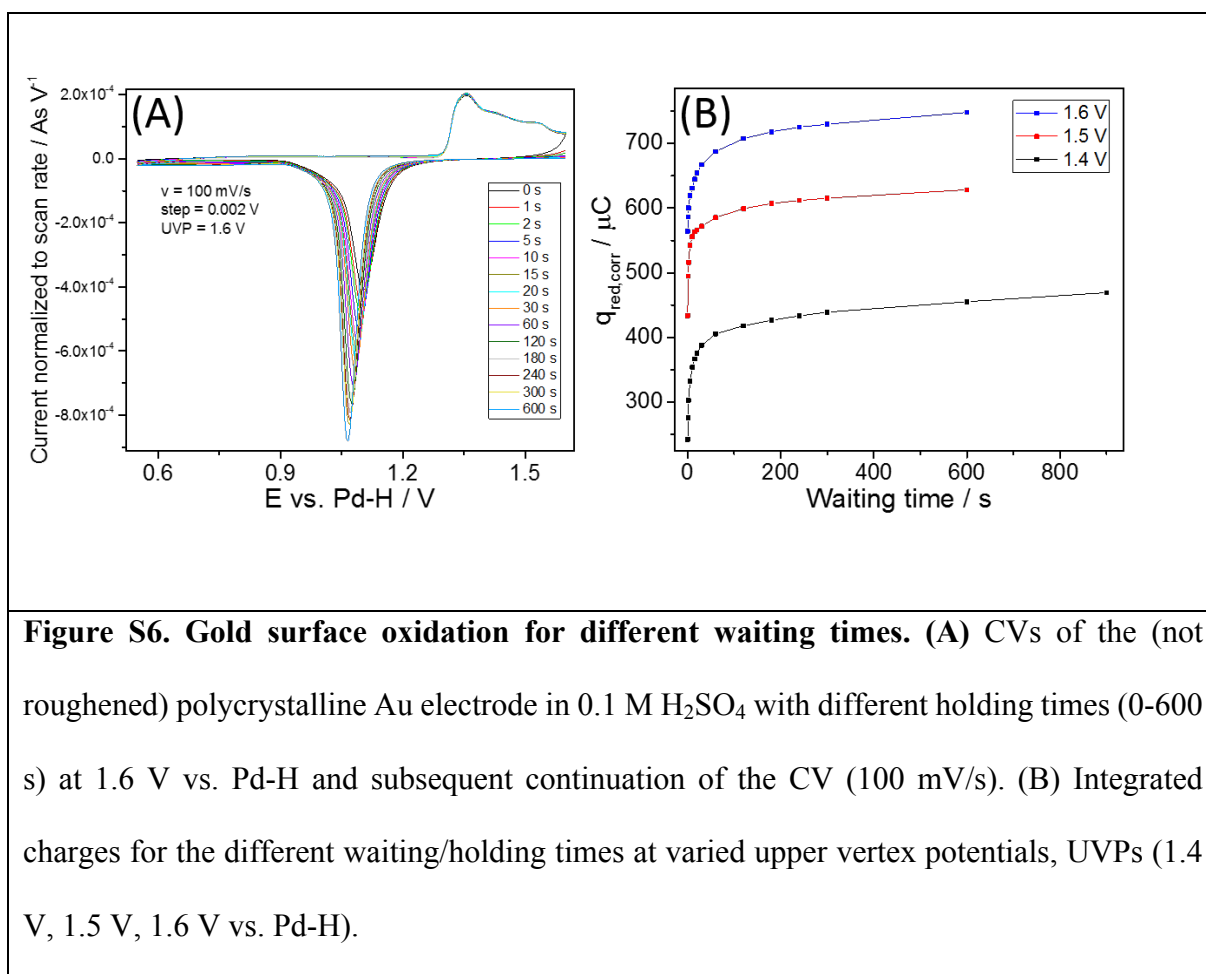
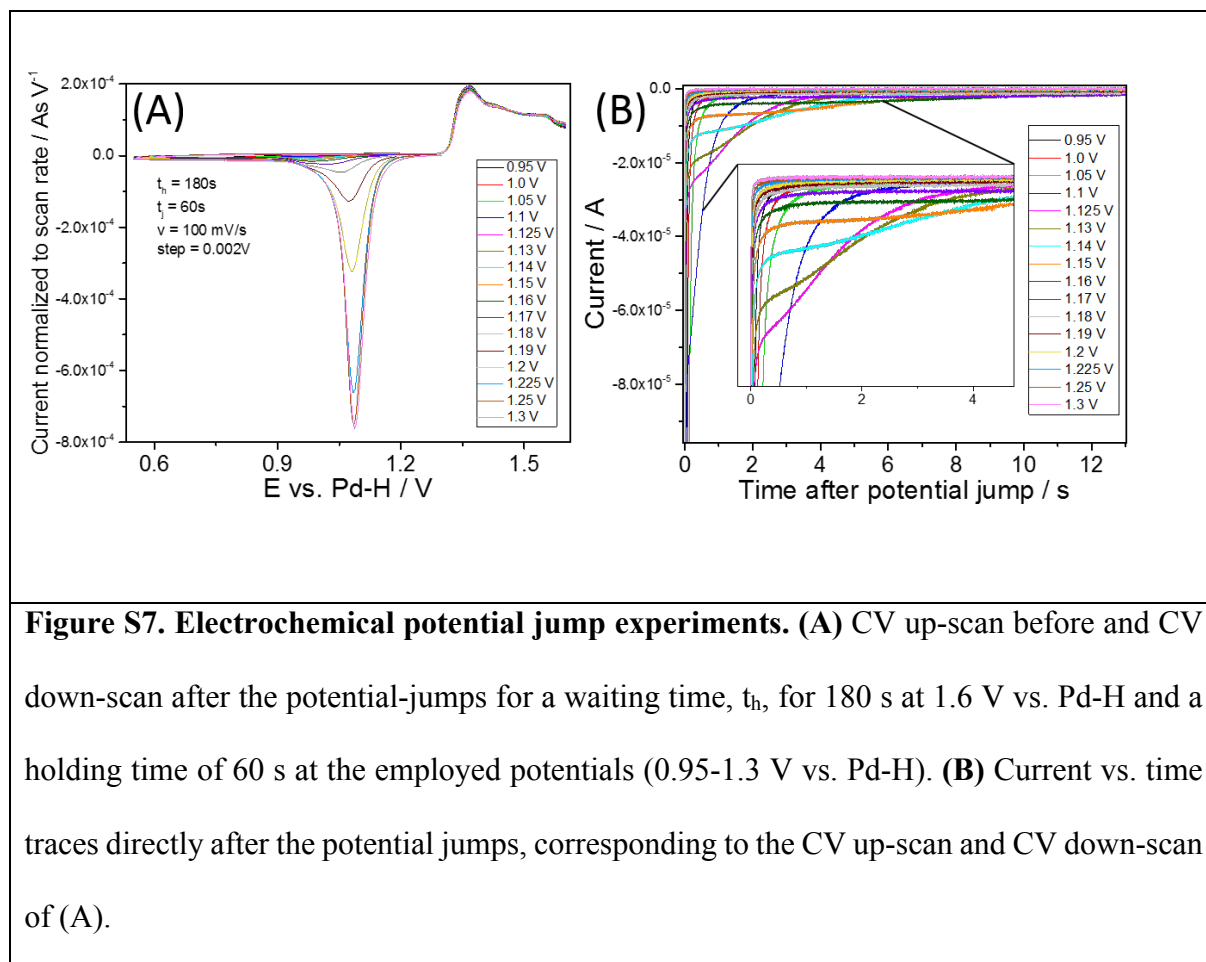


Figure S6. Gold surface oxidation for different waiting times. (A) CVs of the (not roughened) polycrystalline Au electrode in 0.1 M H₂SO₄ with different holding times (0-600 s) at 1.6 V vs. Pd-H and subsequent continuation of the CV (100 mV/s). (B) Integrated charges for the different waiting/holding times at varied upper vertex potentials, UVPs (1.4 V, 1.5 V, 1.6 V vs. Pd-H).

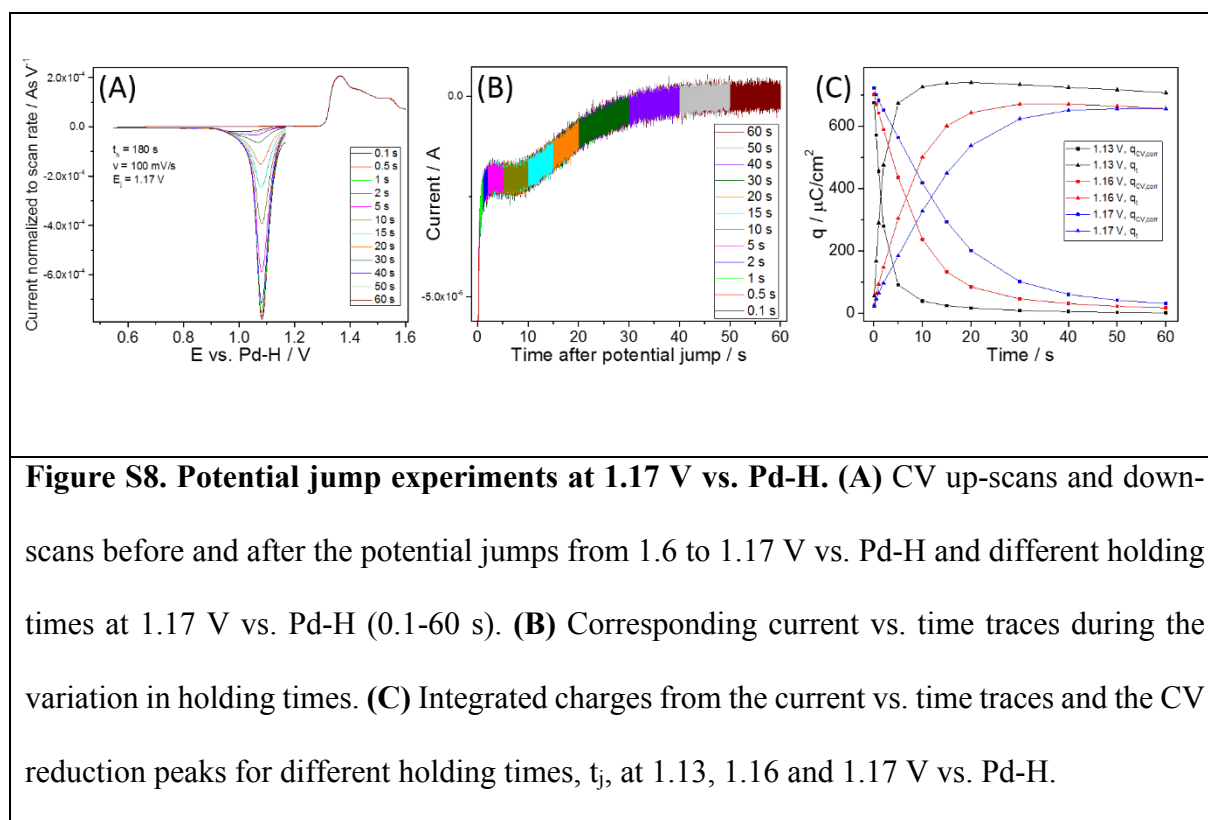
Figure S7A shows the linear potential up-scan to the UVP of 1.6 V vs. Pd-H, which was held for 180 s. The subsequent applied potential in the range from 0.95 to 1.3 V vs. Pd-H was held for 60 s and the following linear potential down-scan is also shown in Figure S7A. The reduction peak increases above 1.125 V vs. Pd-H; for lower potentials, the surface is fully reduced when the applied constant potentials are held for 60 s. Above 1.125 V vs. Pd-H, the reduction peak increases as the applied potential for 60 s is not sufficient to completely reduce the oxidized gold surface. At ~1.25 V vs. Pd-H and above, the full AuOx reduction occurs during the potential down-scan to more negative potentials. With the increase in gold oxide reduction during the CV down-scan, the peak position clearly shifts to more positive potentials. Interestingly, the current vs. time traces recorded after the potential jump from 1.6 V vs. Pd-H exhibit a peculiar shape in the range between 1.1 and 1.19 V vs. Pd-H. In particular, the measured current follows an exponential decay profile only for short times. A current ‘plateau’

is subsequently reached, followed by slow saturation approaching zero current (Figure S7B). Such a behavior clearly suggests a reduction mechanism composed of several processes within the applied potential range.



Further potential jump experiments were performed with different holding times of the specifically applied reduction potential (Figure S8). Figure S8A shows the resulting CV curves for different holding times ($t_j = 0.1$ -60 s). Figure S5B shows the resulting current vs. time traces revealing the previously mentioned ‘current plateau’. Charge integration of the CV reduction peak, $q_{cv,corr}$ (‘corr’ indicates that a calibration factor was employed as will be discussed below, linear sweep vs. small incremental steps), and the charges detected during the applied reduction potentials, q_t , are plotted as a function of time in Figure S8C. As expected, while $q_{cv,corr}$ decreases with increasing t_j , q_t increases approximately in the same fashion. With increasing

reduction potentials (from 1.13 to 1.17 V vs. Pd-H, Figure S8C), an increased holding time is required to fully reduce the AuOx surface, as the reaction proceeds more slowly.



Fitting of I(t) current-time traces during AuOx reduction

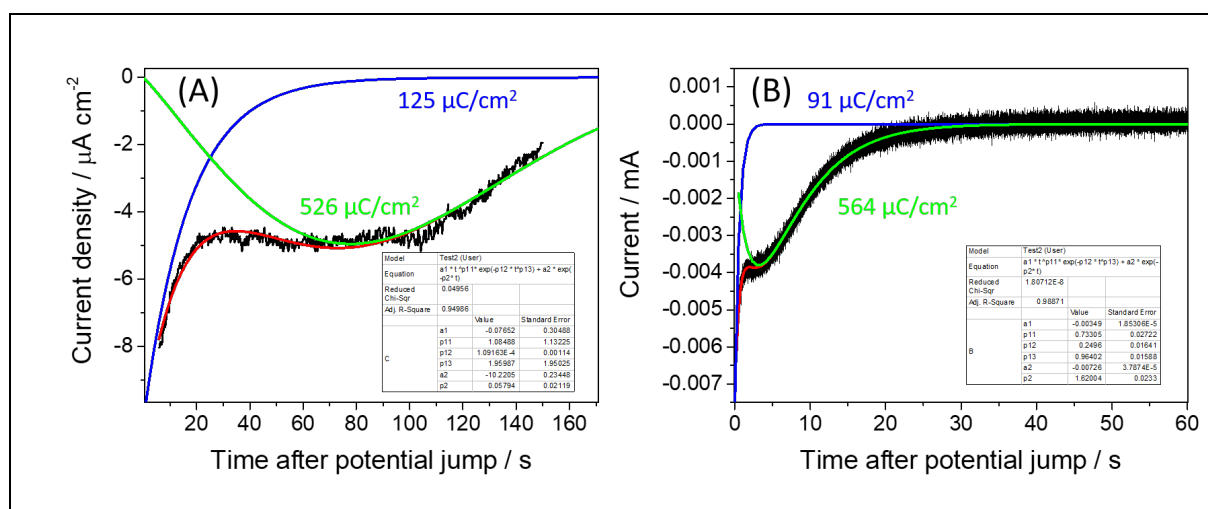


Figure S9. Fitting of current versus time traces during AuO_x reduction. (A) I(t) trace recorded at 1.25 V vs. Pd-H on an electrochemically roughened (SERS-active) polycrystalline Au electrode in D₂O-based 0.1 M H₂SO₄ electrolyte. (B) I(t) trace recorded at 1.16 V vs. Pd-H on an unroughened polycrystalline Au electrode in H₂O-based 0.1 M H₂SO₄ electrolyte.

EC-SERS spectral evolution with time during potential jumps

Example EC-SERS raw spectra recorded after the potential jump from 1.65 to 1.25 V vs. Pd-H in D₂O-based 0.1 M H₂SO₄ electrolyte are portrayed in Figure S10A. The acquisition time accounted to 0.5 s for each spectrum, which are y-offset from another for clarity. The filter cut-off at 156 cm⁻¹ is visible, as well as the spectral features assigned to reaction intermediates. Figure S10B shows two averaged EC-SER spectra obtained by averaging the first 60 spectra (acquisition time ~0.5 s) after the potential jump from 1.6(5) to 1.2(5) V vs. Pd-H in H₂O- and D₂O-based 0.1 M H₂SO₄ electrolytes, respectively.

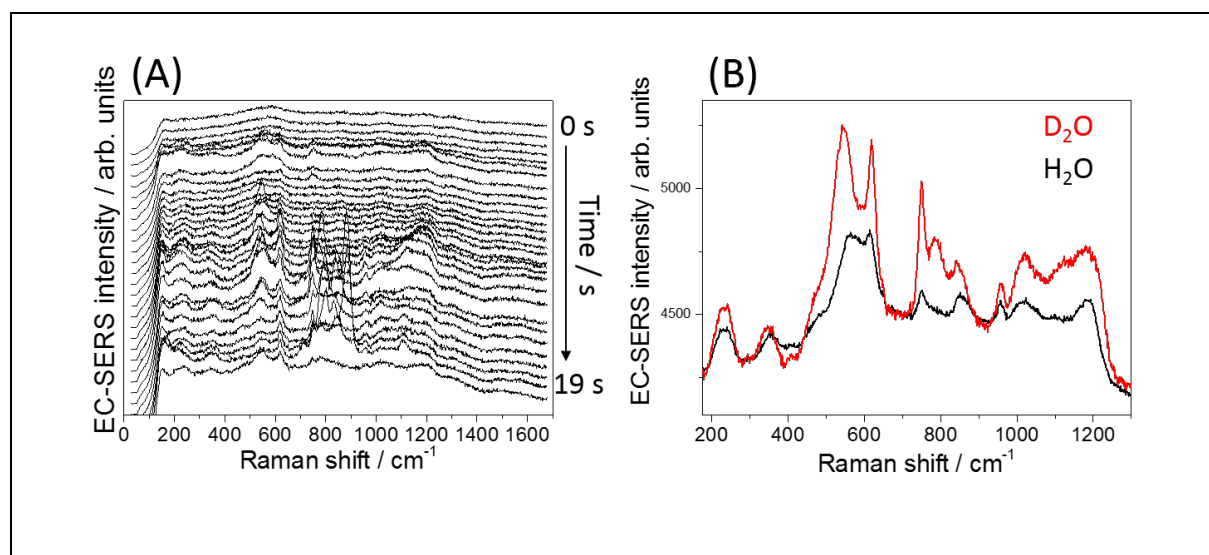


Figure S10. EC-SERS example raw and averaged raw spectra. (A) EC-SER spectral evolution with time after the potential jump from 1.65 to 1.25 V vs. Pd-H in D₂O-based 0.1 M H₂SO₄ electrolyte. (B) Averaged first 60 raw spectra (acquisition time ~0.5 s) after the

potential jump from 1.6(5) to 1.2(5) V vs. Pd-H in H₂O- and D₂O-based 0.1 M H₂SO₄ electrolytes. Spectra are y-offset for clarity.

EC-SERS data analysis and peak fitting procedure

The peak positions from the EC-SERS jump experiments, listed in Table 1 of the main manuscript, were extracted from averaged EC-SER spectra from the first 60 or 30 single spectra recorded after the potential jump from Au oxidation to 1.2(5) V vs. Pd-H for acquisition times of 0.5 or 1 s, respectively. A linear background (autozero = 1) was subtracted and Lorentzian peak fitting was performed with matlab software (peakfit.m, matlab file exchange). The following peak regions were considered: 182-282 cm⁻¹ (single peak); 296-396 cm⁻¹ (single peak); 416-686 cm⁻¹ (double peak); 711-914 cm⁻¹ (triple peak); 934-977 cm⁻¹ (single peak); 975-1272 cm⁻¹ (triple peak). For the broad and asymmetric peak around 594 cm⁻¹ at 1.6 V vs. Pd-H, a peak region of 402-737 cm⁻¹ was fitted with the least number of peaks to give a reasonable fit (determined to be 3 peaks). In addition, we have simply determined the peak maximum as shown in Table S1. For the reliable comparison of H₂O and D₂O data sets, the EC-SERS measurements were always performed subsequently on the same day in H₂O- and D₂O-based sulfuric acid electrolytes with the same sample electrode. For Figure 1C,D, single EC-SER spectra were fitted employing the same matlab code and procedure.

Peak position determination	Peak position in H ₂ O	Peak position in D ₂ O	Δpeak position
Max. value	593.8 ± 6.4 cm ⁻¹	589.2 ± 6.6 cm ⁻¹	within SD
1st peak	488.0 ± 2.1 cm ⁻¹	487.3 ± 1.1 cm ⁻¹	within SD
2nd peak	537.9 ± 5.4 cm ⁻¹	541.2 ± 2.1 cm ⁻¹	within SD
3rd peak	599.2 ± 2.6 cm ⁻¹	597.3 ± 1.5 cm ⁻¹	within SD

Table S1. Determined peak positions at 1.6 V vs. Pd-H in H₂O and D₂O solutions. AuOx peak positions at 1.6(5) V vs. Pd-H determined either as maximum peak value or triple Lorentzian peak fit (see text for details). SD stands for standard deviation.

Figure S11A-F and Figure 1B show contour plots of EC-SERS spectral evolution as a function of time. The images were constructed by plotting the acquired EC-SERS single spectra as a function of time after subtraction of an asymmetric least square background (matlab, `asLS_baseline_v1.m`, smoothness parameter = $1e2$, break iterations if difference is less than $1e-6$).¹³

Figure S11A shows the EC-SERS spectral evolution with time at 1.25 V vs. Pd-H before jumping to the gold oxide formation. Figure S11B reveals the spectral evolution at 1.65 V vs. Pd-H and the appearance of the broad and asymmetric peak around 594 cm^{-1} due to AuOx. Figure S11C-F compares the EC-SER spectral evolution at the onset reduction potential of AuOx at $\sim 1.2\text{ V}$ vs. Pd-H. Strong spectral features, in comparison to Figure S11A, are apparent and identified as temporarily detected reaction intermediates. By comparing different rounds of experiments (Figure S11C-F), it is evident that the spectral features are well reproducible; however, oxidation/reduction cycles also change the nanostructure surface composition that will result into differences in the temporal appearance of the different spectral features (e.g. $750\text{-}850\text{ cm}^{-1}$ region). It is important to note that since multiple hotspots can possibly contribute to the acquired signal, the EC-SER spectra as a function of time do not necessarily reflect the temporal order of the observed reaction intermediates.

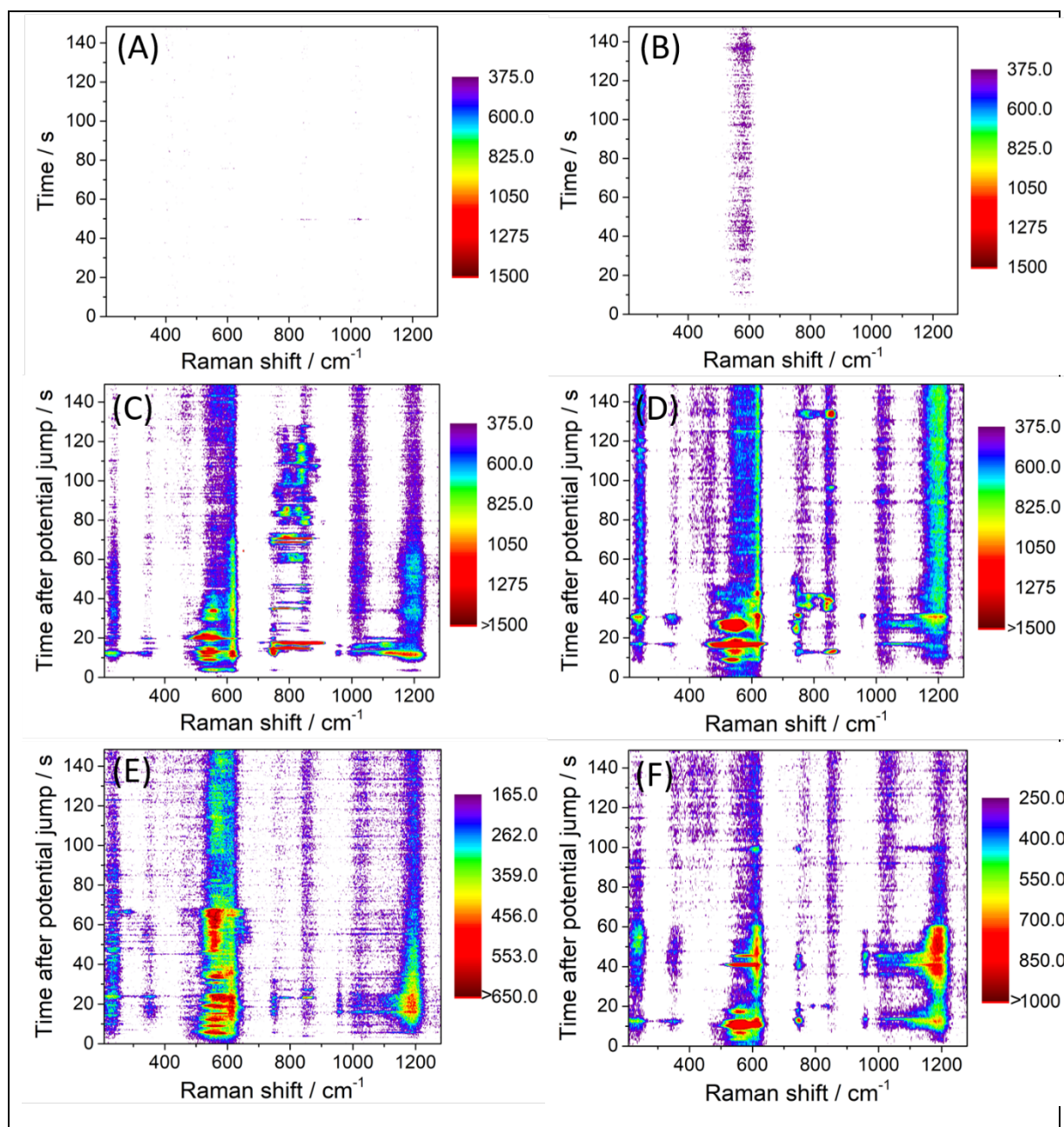


Figure S11. EC-SER spectral evolution with time. (A) EC-SER spectra recorded at 1.25 V vs. Pd-H before jumping to surface oxidation at 1.65 V vs. Pd-H. (B) EC-SER spectra recorded as a function of time at 1.65 V vs. Pd-H. A broad and asymmetric peak around 594 cm^{-1} appears due to oxide/hydroxide structures. (C-F) EC-SERS spectral evolution with time at 1.25 V vs. Pd-H in D_2O -based (C, D) and at 1.65 V vs. Pd-H in H_2O -based (E, F) sulfuric acid electrolytes. Spectral acquisition times: 0.5 s (A-C, E); 1 s (D, F).

Table S2. Highest frequencies computed for Au-OH/D and AuOx. (Upper panel) Au-OH/D stretch frequencies calculated for the structures involving adsorbed OH/D illustrated in Figure S12A-C. **(Lower panel)** Maximum frequencies calculated for the oxygen containing structures illustrated in Figure S12D-L.

Interface	Interface structure	Au-OH/D frequency (vacuum, cm^{-1})	Au-OH/D frequency (solvent, cm^{-1})
(A)	Au(111) (bridge site)	328/322	316/312
(B)	Au adatom (atop)	558/534	531/517
(C)	Au row (bridge site)	371/365	361/358

Interface	Interface structure	Max. frequency (vacuum, cm^{-1})	Max. frequency (solvent, cm^{-1})
(D)	Au(111) + 1/4 ML	384	381
(E)	Au(111) + 2/4 ML	446	442
(F)	Au(111) + 3/4 ML	437	441
(G)	Au(111) + 4/4 ML	581	583
(H)	Au(111) + AuO ₂	600	599
(I)	Au(111) + Au ₂ O	482	480
(J)	Au(111) + Au ₂ O ₂	585	585
(K)	Au(111) + Au ₂ O ₃	594	601
(L)	Au(111) + Au ₂ O ₄	609	621

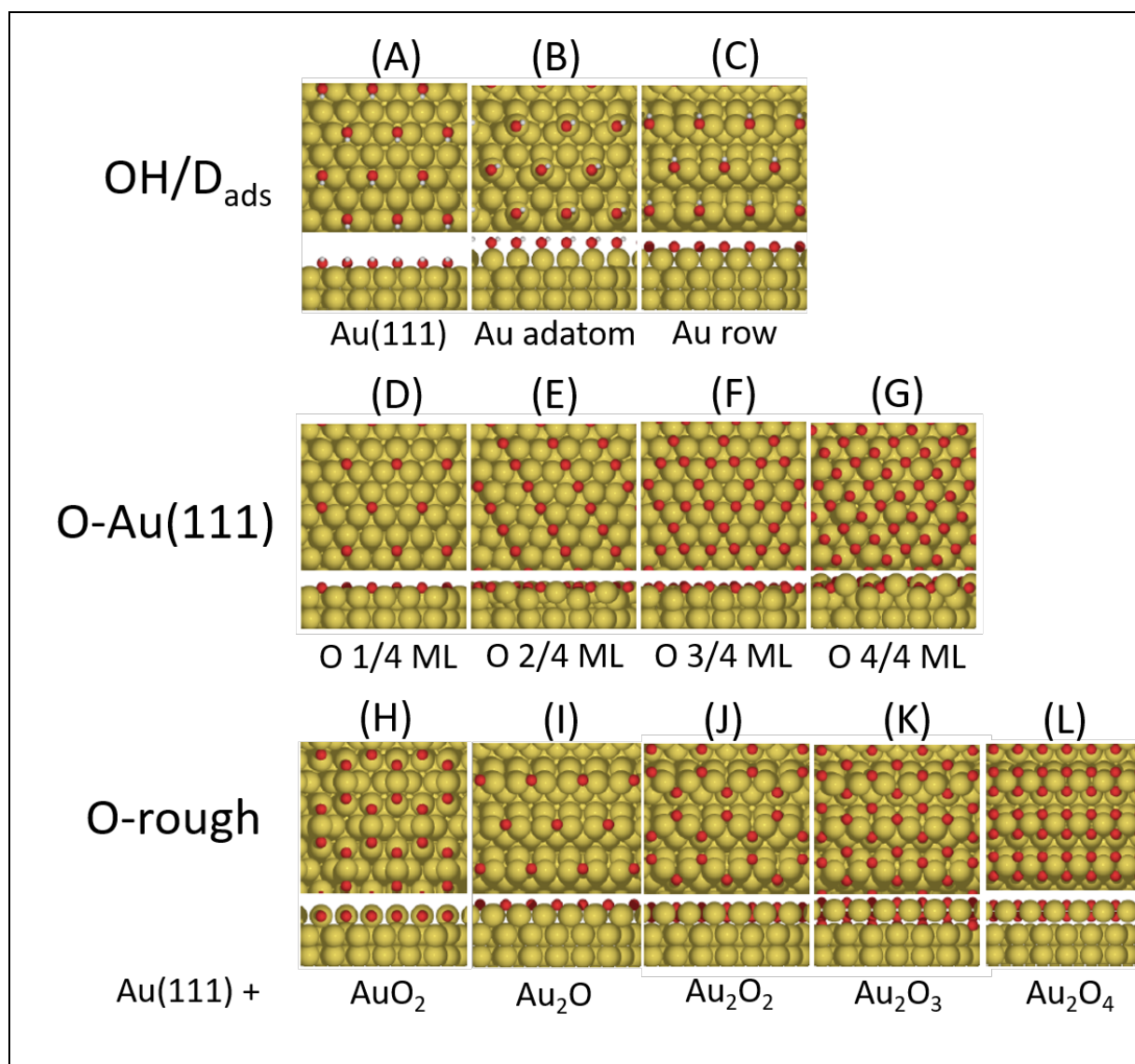
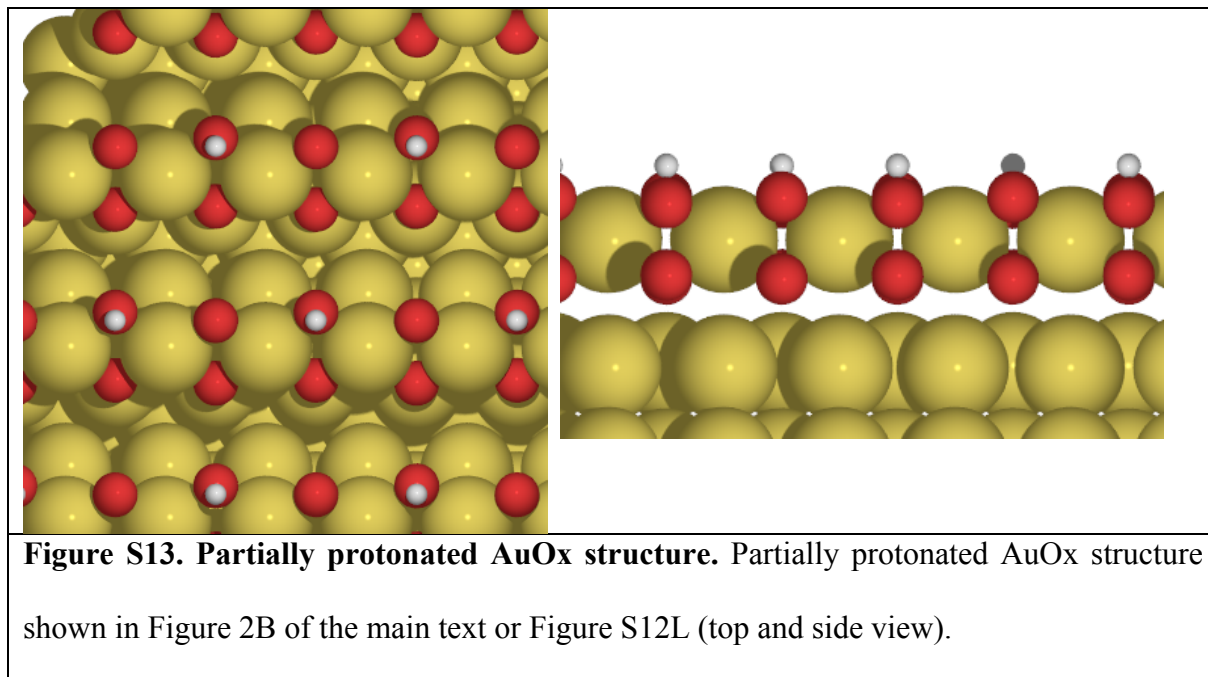


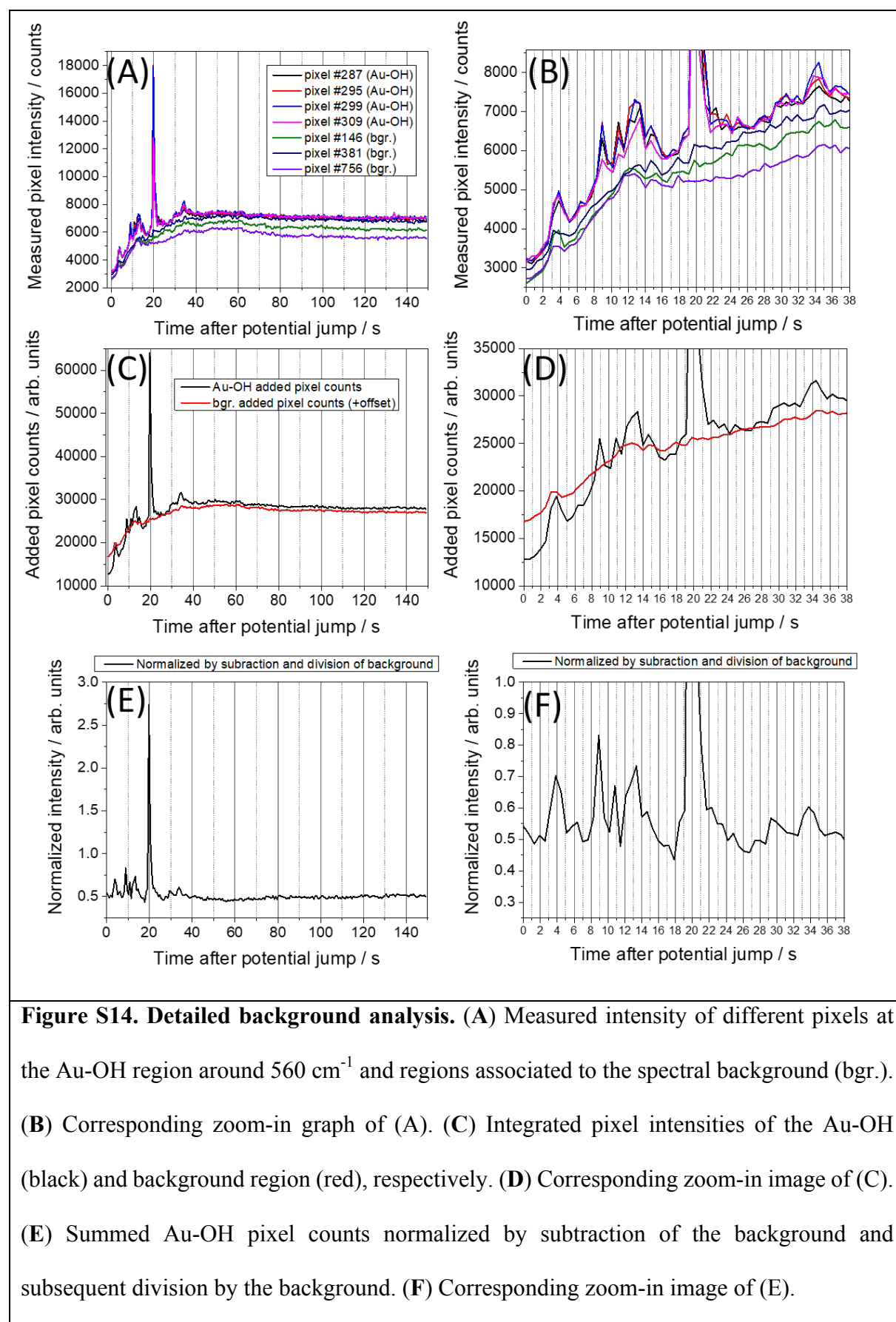
Figure S12. Illustration of the most stable interface structures for the calculations of Au-OH and AuOx vibrational frequencies. Oxygen, hydrogen and gold atoms are shown in red, grey and yellow, respectively. For each structure, top and side views are presented. **(A-C)** Most stable OH-adsorption configurations on the flat and roughened gold surfaces according to geometry optimization. **(D-G)** Illustration of the partially oxidized structures originating from a flat Au(111) surface. **(H-L)** Structures originated from 'roughened' surfaces (i.e. including one or two gold adatoms) with different amounts of oxygen atoms.

Partially protonated AuOx structure

Figure S13 shows the partially protonated AuOx structure that is illustrated in Figure 3L of the main manuscript. The partially protonated structure (with H and D, respectively), also employed for DFT calculations, explains the experimentally observed up-shift of the 613 cm^{-1} peak that is observed going from H_2O - to D_2O -based electrolyte.

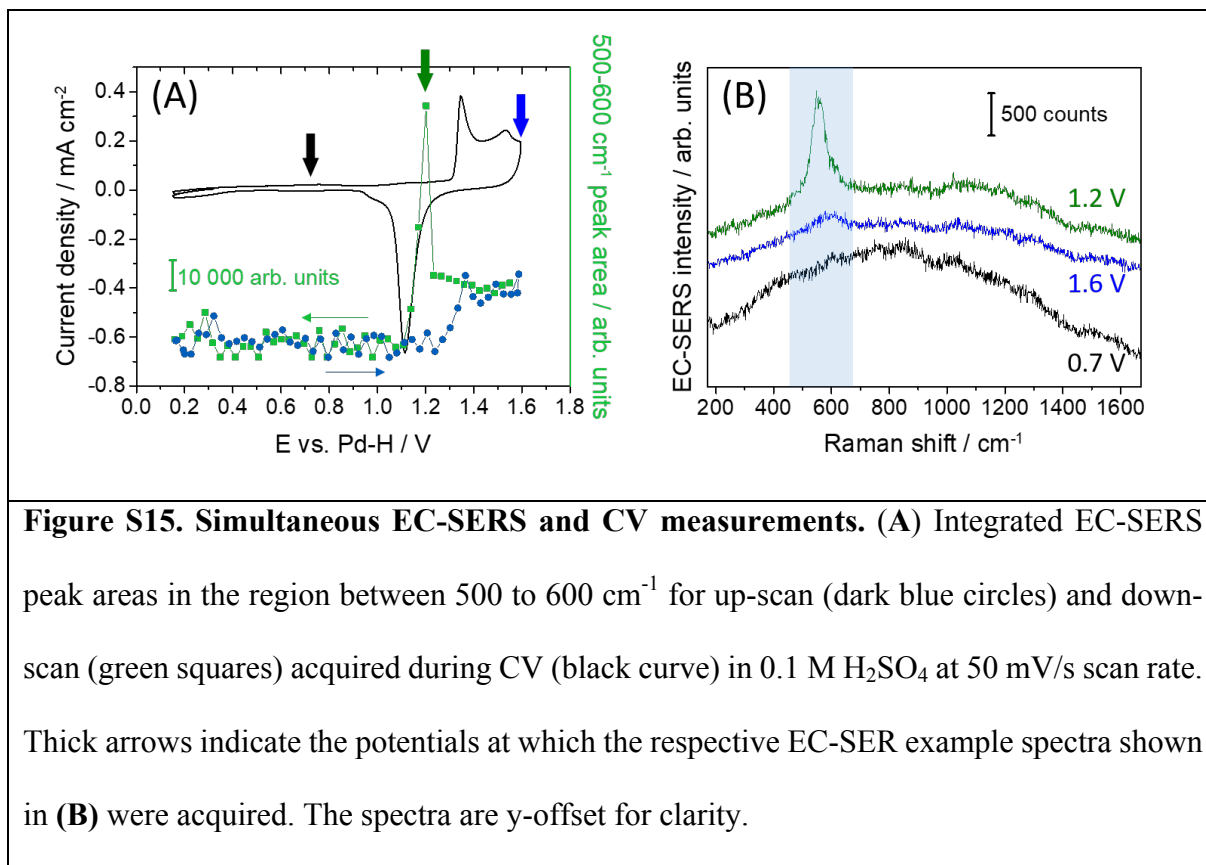


Analysis of the EC-SERS background



EC-SERS during CV measurements

Figure S15A shows the CV of the roughened polycrystalline gold electrode recorded in the EC-SERS cell at a scan rate of 50 mV/s in 0.1 M H₂SO₄. The oxidation of the polycrystalline Au electrode starts at ~1.3 V vs. Pd-H and the subsequent reduction of surface AuOx commences at around 1.2 V vs. Pd-H. The obtained CV is in accordance with the literature^{14–16} and corresponds well with additional electrochemical measurements on polycrystalline gold without the roughening procedure necessary to provide SERS enhancement (Figure S5). Figure S15B shows example EC-SER spectra acquired at different electrode potentials during CV. While at 0.7 V vs. Pd-H, no peaks are apparent on top of the broad SERS background, at 1.6 V vs. Pd-H an asymmetric peak around 594 cm⁻¹ is visible. During the cathodic scan toward more negative potentials, an intense peak around ~560 cm⁻¹ is observed at the onset of the AuOx reduction (~1.2 V vs. Pd-H) that differs in peak position and intensity from the broad asymmetric peak around 594 cm⁻¹. The integrated peak intensity of the spectral region between 450 to 650 cm⁻¹ (Figure S15A, blue dots and green squares for up- or down-scan, respectively) displays the growth of the 594 cm⁻¹ peak during surface oxidation from around 1.3 V vs. Pd-H to a plateau intensity between 1.4 and 1.6 V vs. Pd-H. During the reverse scan, the EC-SERS signal rises intensively at around 1.2 V vs. Pd-H and then vanishes below 1.1 V vs. Pd-H while scanning further toward more negative potentials.

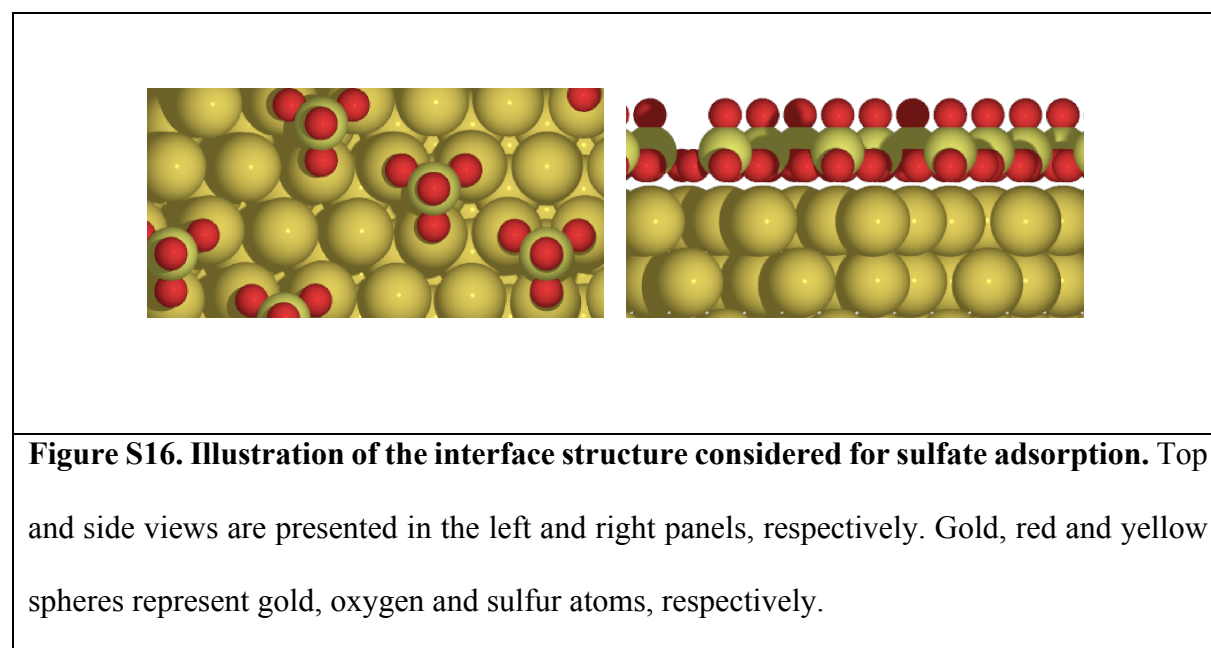


Frequency calculations for adsorbed sulfate

Tri-dentate sulfate adsorption on Au(111) has been simulated using a $(\sqrt{3} \times \sqrt{7})$ supercell of the substrate unit cell (see Figure S13). The modeled ad-layer reproduces the structure that has been experimentally observed on a Au(111) single-crystal electrode with combined infrared and scanning tunneling microscopy.¹⁷ A Γ -centered (4x6x1) k-point grid has been employed to sample the IBZ, while all other computational parameters have been taken as identical to the ones described in the methods section of the main paper. The frequencies computed for the S-O stretching modes are reported in Table S3, while all other modes have been found to have a frequency lower than 580 cm^{-1} .

The vibrational frequencies of the tri-dentate sulfate structure on Au(111) were calculated based on implicit solvent calculations. It is worthwhile to note that in a recent study that included explicit water molecules in addition to an implicit solvent, Gossenberger et al. found that such

adlayer structure of tri-dentately adsorbed sulfate species is the most stable sulfate adsorption configuration under high-potential condition.¹⁸



Mode	Frequency (vacuum, cm^{-1})	Frequency (solvent, cm^{-1})
S-O (surface)	830, 834, 842	836, 839, 854
S-O (free)	1253	1255

Table S3. Frequencies computed for the S-O stretching for adsorbed sulfate. Frequencies computed in vacuum and in implicit solvent are reported. Stretching modes involving surface-bound oxygen atoms are distinguished from the modes involving surface-free oxygen atoms.

Data acquisition and processing procedure of electrochemical measurements

The Nova 2.1.2 software (for the Metrohm Autolab PGSTAT 30 multipotentiostat) does not provide the means to combine the potential jump experiments with analog linear sweep/cyclic voltammetry measurements. Therefore, a digital staircase voltage profile was utilized, in which the applied potential is adjusted in very small and adaptable step-sizes. Additional test measurements showed that the CV shapes with linear and staircase acquisition match best for a step size of 0.002 V.

To ensure that we obtain the correct absolute charge values from the CV curves, a calibration method was employed: At the start of each set of measurements, a complete CV of the desired potential range was recorded using the linear voltage profile as well as the staircase voltage profile (step size = 0.002 V). The extracted reduction charges were determined and provide a calibration factor to accurately compare the charges during the potential jump and CV experiments, under the assumption that the calibration factor does not change upon adjustment of the potential jump parameters.

The charges from the CVs were determined by subtraction of the local maximum (negative current range) after the reduction peak (to more negative potentials) and before the onset of the double layer currents as constant baseline. Subsequently, the peak area under the reduction peak was integrated. For the jump experiments, the area under the current vs. time traces was determined.

Determination of the 560 cm⁻¹ intensity oscillation frequency

The peak area oscillation frequency of the Au-OH band at ~560 cm⁻¹ was determined by Gaussian peak fitting (OriginPro) of the previously determined peak area as a function of time traces (e.g. Figure 1D of the main manuscript; Figure S17A+B) at 1.2(5) V vs. Pd-H (after

AuOx formation) and determination of the differences of subsequent peak positions. The oscillation frequencies in H₂O and D₂O sulfuric acid electrolytes accounted to 4.0 ± 1.3 s and 4.5 ± 1.9 s, respectively. Following the same procedure, the EC-SERS intensity variations of all (bi)sulfate peaks was analyzed (Figure S17C+D). The (bi)sulfate oscillation frequencies in H₂O and D₂O sulfuric acid electrolytes accounted to 3.9 ± 1.5 s and 5.1 ± 2.3 s, respectively.

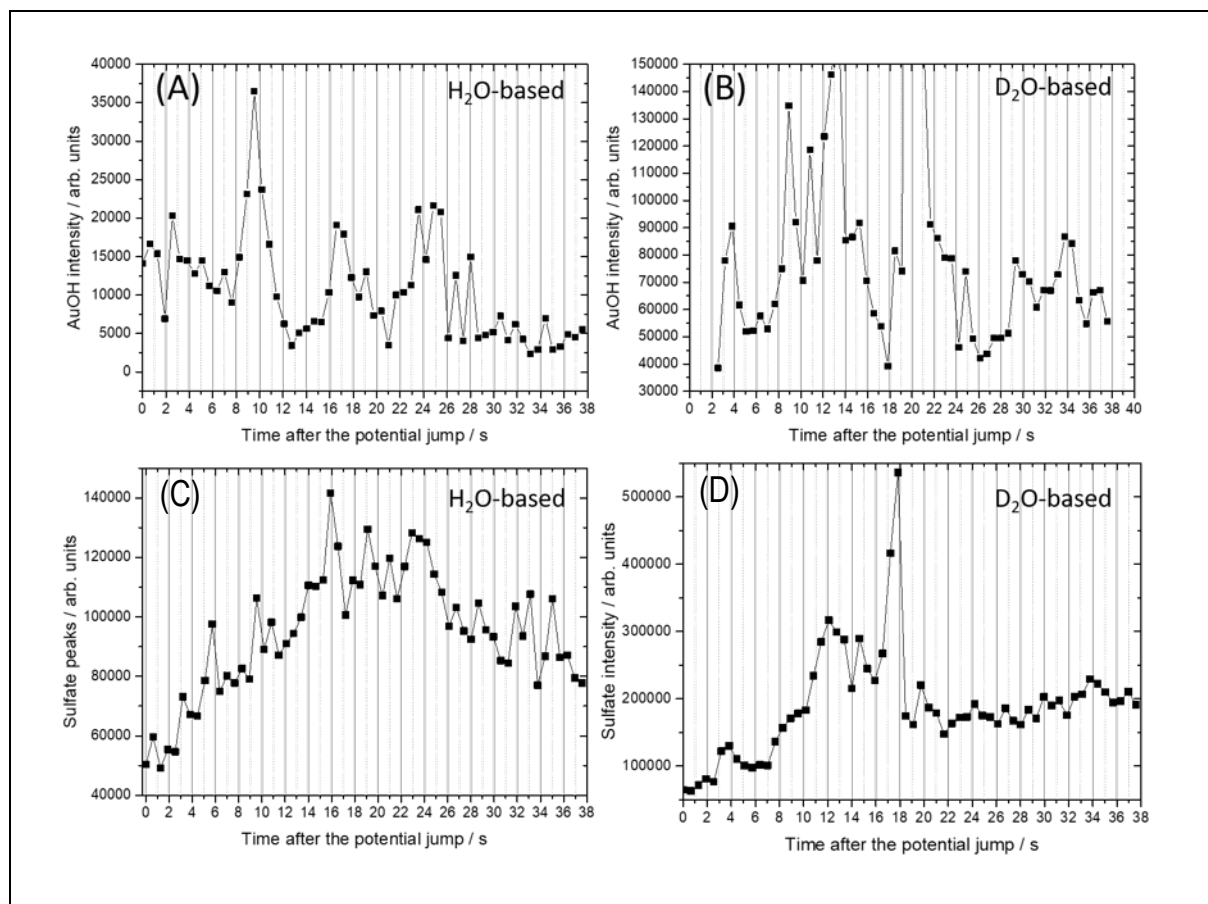


Figure S17. AuOH and sulfate SERS intensity oscillations. (A and B) EC-SERS intensity oscillations of the AuOH peak as a function of time at 1.2(5) V vs. Pd-H after the potential jump from surface oxidation (A: in H₂O-based sulfuric acid electrolyte; B: in D₂O-based sulfuric acid electrolyte). **(C and D)** EC-SERS intensity oscillations of the (bi)sulfate peaks as a function of time at 1.2(5) V vs. Pd-H after the potential jump from Au surface oxidation in H₂O- (C) and D₂O-based (D) electrolyte.

Geometry optimization

For the various surface structures investigated with DFT (surface structures in Figure S12 represent stable surface structures after geometry optimization), geometry optimization has been carried out until all Cartesian components of all forces were smaller than 0.0002 atomic units (Ry/Bohr) with no imaginary frequency. Since the forces are the opposite of the gradient of the energy, having a gradient very close to zero means that the surface structure is close to a minimum.

References

- (1) Nørskov, J. K.; Rossmeisl, J.; Logadottir, A.; Lindqvist, L.; Kitchin, J. R.; Bligaard, T.; Jónsson, H. Origin of the Overpotential for Oxygen Reduction at a Fuel-Cell Cathode. *J. Phys. Chem. B* **2004**, *108* (46), 17886–17892. <https://doi.org/10.1021/jp047349j>.
- (2) Togo, A.; Tanaka, I. First Principles Phonon Calculations in Materials Science. *Scr. Mater.* **2015**, *108*, 1–5. <https://doi.org/10.1016/j.scriptamat.2015.07.021>.
- (3) Hörmann, N. G.; Andreussi, O.; Marzari, N. Grand Canonical Simulations of Electrochemical Interfaces in Implicit Solvation Models. *J. Chem. Phys.* **2019**, *150* (4), 041730–041731. <https://doi.org/10.1063/1.5054580>.
- (4) Andreussi, O.; Dabo, I.; Marzari, N. Revised Self-Consistent Continuum Solvation in Electronic-Structure Calculations. *J. Chem. Phys.* **2012**, *136* (6), 064102–1. <https://doi.org/10.1063/1.3676407>.
- (5) Sundararaman, R.; Letchworth-Weaver, K.; Schwarz, K. A. Improving Accuracy of Electrochemical Capacitance and Solvation Energetics in First-Principles Calculations. *J. Chem. Phys.* **2018**, *148* (14), 1–8. <https://doi.org/10.1063/1.5024219>.
- (6) Nattino, F.; Truscott, M.; Marzari, N.; Andreussi, O. Continuum Models of the Electrochemical Diffuse Layer in Electronic-Structure Calculations. *J. Chem. Phys.* **2019**, *150* (4), 1–17. <https://doi.org/10.1063/1.5054588>.
- (7) Fisicaro, G.; Genovese, L.; Andreussi, O.; Mandal, S.; Nair, N. N.; Marzari, N.; Goedecker, S. Soft-Sphere Continuum Solvation in Electronic-Structure Calculations. *J. Chem. Theory Comput.* **2017**, *13* (8), 3829–3845. <https://doi.org/10.1021/acs.jctc.7b00375>.

- (8) *Modern Aspects of Electrochemistry*, 1st ed.; White, R. E., Bockris, J. O., Conway, B. E., Eds.; Springer US, 1999.
- (9) Borukhov, I.; Andelman, D.; Orland, H. Steric Effects in Electrolytes: A Modified Poisson-Boltzmann Equation. *Phys. Rev. Lett.* **1997**, *79* (3), 435–438. <https://doi.org/10.1103/PhysRevLett.79.435>.
- (10) Nightingale, E. R. Phenomenological Theory of Ion Solvation. Effective Radii of Hydrated Ions. *J. Phys. Chem.* **1959**, *63* (9), 1381–1387. <https://doi.org/10.1021/j150579a011>.
- (11) Clavilier, J.; Van Huong, C. N. Etude de L'interface de L'or Polycristallin Au Contact de Solutions Aqueuses de Perchlorate de Potassium et D'acide Perchlorique. *J. Electroanal. Chem.* **1977**, *80* (1), 101–114. [https://doi.org/10.1016/S0022-0728\(77\)80106-X](https://doi.org/10.1016/S0022-0728(77)80106-X).
- (12) Tremiliosi-Filho, G.; Dall'Antonia, L. H.; Jerkiewicz, G. Limit to Extent of Formation of the Quasi-Two-Dimensional Oxide State on Au Electrodes. *J. Electroanal. Chem.* **1997**, *422* (1-2), 149–159. [https://doi.org/10.1016/S0022-0728\(96\)04896-6](https://doi.org/10.1016/S0022-0728(96)04896-6).
- (13) Eilers, P. H. C. A Perfect Smoother. *Anal. Chem.* **2003**, *75* (14), 3631–3636. <https://doi.org/10.1021/ac034173t>.
- (14) Yeo, B. S.; Klaus, S. L.; Ross, P. N.; Mathies, R. A.; Bell, A. T. Identification of Hydroperoxy Species as Reaction Intermediates in the Electrochemical Evolution of Oxygen on Gold. *ChemPhysChem* **2010**, *11* (9), 1854–1857. <https://doi.org/10.1002/cphc.201000294>.
- (15) Diaz-Morales, O.; Calle-Vallejo, F.; De Munck, C.; Koper, M. T. M. Electrochemical Water Splitting by Gold: Evidence for an Oxide Decomposition Mechanism. *Chem. Sci.* **2013**, *4* (6), 2334–2343. <https://doi.org/10.1039/c3sc50301a>.
- (16) Cherevko, S.; Topalov, A. A.; Zeradjanin, A. R.; Katsounaros, I.; Mayrhofer, K. J. J. Gold Dissolution: Towards Understanding of Noble Metal Corrosion. *RSC Adv.* **2013**, *3* (37), 16516–16527. <https://doi.org/10.1039/c3ra42684j>.
- (17) Edens, G. J.; Gao, X.; Weaver, M. J. The Adsorption of Sulfate on gold(111) in Acidic Aqueous Media: Adlayer Structural Inferences from Infrared Spectroscopy and Scanning Tunneling Microscope. *J. Electroanal. Chem.* **1994**, *375* (1-2), 357–366. [https://doi.org/10.1016/0022-0728\(94\)03420-6](https://doi.org/10.1016/0022-0728(94)03420-6).
- (18) Gossenberger, F.; Juarez, F.; Groß, A. Sulfate, Bisulfate, and Hydrogen Co-Adsorption on Pt(111) and Au(111) in an Electrochemical Environment. *Front. Chem.* **2020**, *8* (July), 1–11. <https://doi.org/10.3389/fchem.2020.00634>.